

# Eigenstructure Analysis of Bloch Wave and Multislice Matrix Formulations for Dynamical Scattering in Transmission Electron Microscopy

Arya Bangun<sup>1</sup>, Oleh Melnyk<sup>2</sup>, Benjamin März<sup>3</sup>

## Abstract

We investigate the eigenstructure of matrix formulations used for modeling scattering processes in materials by transmission electron microscopy (TEM). Considering dynamical scattering is fundamental in describing the interaction between an electron wave and the material under investigation. In TEM, both the Bloch wave formulation and the multislice method are commonly employed to model the scattering process, but comparing these models directly is challenging. Unlike the Bloch wave formulation, which represents the transmission function in terms of the scattering matrix, the traditional multislice method does not have a pure transmission function due to the entanglement between electron waves and the propagation function within the crystal. To address this, we propose a reformulation of the multislice method into a matrix framework, which we refer to as transmission matrix. This enables a direct comparison to the well-known scattering matrix, derived from the Bloch wave formulation, and analysis of their eigenstructures. We show theoretically that both matrices are equal, under the condition that the angles of the eigenvalues differ no more than modulo  $2\pi n$  for integer  $n$ , and the eigenvectors of the transmission and scattering matrix are related in terms of a two-dimensional Fourier matrix. The characterization of both matrices in terms of physical parameters, such as total projected potentials, is also discussed, and we perform numerical simulations to validate our theoretical findings. Finally, we show that the determinant of the transmission matrix can be used to estimate the mean inner potential.

## 1 Introduction

Modeling the three-dimensional atomic structure of a material is essential for studying its physical characteristics and atomic electrostatic potential which can significantly aid in the process of structure retrieval from experimental data, i.e., diffraction patterns, when observing the material in instruments such as electron microscopes. Determining the crystalline structure of materials from diffraction experiments is inseparable from the theory of multiple electron scattering, developed by Bethe [1]. Since then, numerous formulations have been developed to model multiple scattering phenomena in crystals, including the multislice method [2–5] and the scattering matrix obtained from Bloch waves [6, 7]. Both models are frequently used for model-based reconstruction in transmission electron microscopy (TEM), as for example discussed in [8–16].

Formulating the scattering matrix from the Bloch wave method essentially incorporates the superposition of many periodic waves within a crystal to solve the Schrödinger equation. Therefore, the relation between electrostatic potential and Bloch waves within the crystal can be represented by an eigenvalue problem. Consequently, the scattering matrix is described by its eigenvalue decomposition, with the eigenvalues encoding parameters such as the specimen’s thickness, and the eigenvectors providing the Fourier coefficients of Bloch waves. On the other hand, the multislice method approximates the scattering processes of an incident electron wave when interacting with the electrostatic potential of the crystal by treating many thin slices of projected atomic potentials consecutively, with the exit wave of one slice is used as the input wave for the following.

The relationship between Bloch waves and the multislice method has been discussed, for instance in [17]. The scattering matrix is expressed in terms of the matrix exponential of the crystal structure matrix, which in turn is decomposed into phase grating and propagation operator terms. However, the challenge in separating both operators lies in the non-commutative nature of the matrix product, making

<sup>1</sup> IAS-8, Forschungszentrum Jülich, Germany, <sup>2</sup>Department of Mathematics, TU Berlin, Germany,

<sup>3</sup> Shared Instrumentation Facility, Louisiana State University, USA

a simple decomposition valid only by applying the first-order Taylor approximation, which is the core idea of the multislice method. This approximation requires the slice thickness to be small, in order to ensure sufficient accuracy.

Although the derivation of multislice is straightforward, it is difficult to quantify any differences between the Bloch wave formulation and the multislice method when modeling scattering processes in crystalline materials. Several approaches have been discussed to numerically compare both models, for instance as discussed in [18–21]. However, apart from the computation time, these analyses are mainly focused at the error in the amplitude of the specimen exit wave functions for both the Bloch wave and the multislice methods for various crystalline materials.

While such comparisons are valid to capture the performance, accuracy and consistency of the results of both models, it treats the model as a black box system and measures the similarity implicitly in terms of the output only. More importantly, measuring similarity solely based on intensity only captures the projection information, which does not provide insight into the spatial structure of the electrostatic potentials, neither in the Bloch wave nor the multislice approach. In our study, we go a step further and, rather than relying on the projected intensity alone, we directly evaluate the 3D electrostatic potential.

In the original formulation of the multislice method, the possibility of defining a pure transmission functions, akin to the scattering matrix in the Bloch wave approach, is precluded due to the inherent entanglement between the exit wave across slices and Fresnel propagation. As a consequence, a direct comparison of the eigenstructure of the scattering matrix with the multislice method is not possible. For this reason, we reformulate the multislice model using matrix products and achieve a crucial separation between the input wave and the matrix that represents the transmission function of the crystal structure, which we call *transmission matrix*. This reformulation enables us to model the transmission function in a manner directly comparable to the scattering matrix by using eigenstructure analysis. Rather than the conventional approach of comparing resulting intensities, we present a direct mathematical comparison of the transmission matrix with the scattering matrix. Furthermore, we investigate whether the similarity between both matrices implies that also the underlying atomic structure is the same by evaluating diffraction data simulated by both methods. Apart from measuring the similarity between transmission and scattering matrix, we also leverage the determinant (the product of eigenvalues) of the transmission matrix to estimate the mean inner potential (MIP).

**Summary of Contributions.** We discuss the structural similarity between a matrix obtained using the Bloch wave formulation in comparison to a matrix realized through the multislice method, which throughout this article we refer to as *scattering matrix* and *transmission matrix*, respectively. We follow the construction of the transmission matrix, as discussed in [15], and eliminate the dependency on, and the entanglement with, the input wave. Hence, its eigenstructure can be evaluated and compared to the scattering matrix of the Bloch wave method. The equivalence of both matrices is investigated by leveraging their eigenstructures, i.e., their eigenvalues and eigenvectors. We discuss how this equivalency provides insights into the underlying physical processes of dynamical scattering and the accuracy of the approximations made in each method. We provide numerical simulations to generate atomic potentials and scattering matrices, calculated directly from the multislice and Bloch wave models. Additionally, we perform the comparison by visualizing the distribution of eigenvalues, present plane-wave diffraction patterns and compare the estimated projected potential. We also demonstrate a novel approach to estimate the MIP by using the product of the eigenvalues, i.e., the determinant, of the transmission matrix.

**Notations** Vectors are written in bold small-cap letters  $\mathbf{x} \in \mathbb{C}^L$  and matrices are written in bold big-cap letters  $\mathbf{A} \in \mathbb{C}^{K \times L}$  for a complex field  $\mathbb{C}$  and  $\mathbb{R}$  for a real field. Matrices can also be written as its element  $\mathbf{A} = (a_{k\ell})$ , where  $k \in [K], \ell \in [L]$ . The set of integers is written as  $[N] := \{1, 2, \dots, N\}$  and calligraphic letters are used to define functions  $\mathcal{A} : \mathbb{C} \rightarrow \mathbb{C}$ . Specifically, we denote the discrete two-dimensional Fourier transform by  $\mathcal{F}$ . For both matrices and vectors the notation  $\circ$  is used to represent the element-wise or Hadamard product. The  $\mathbf{A}^H$  is used to represent conjugate transpose. A matrix is called unitary if  $\mathbf{A}^H \mathbf{A} = \mathbf{A} \mathbf{A}^H = \mathbf{I}$ , where  $\mathbf{I}$  is the identity matrix. For a matrix  $\mathbf{A} \in \mathbb{C}^{K \times L}$ , the Frobenius norm is given by  $\|\mathbf{A}\|_F = \left( \sum_{k=1}^K \sum_{\ell=1}^L |a_{k\ell}|^2 \right)^{1/2} = (\text{trace}(\mathbf{A}^H \mathbf{A}))^{1/2}$ .

Code: [https://github.com/bangunarya/eigenstructure\\_bloch\\_ms](https://github.com/bangunarya/eigenstructure_bloch_ms)

## 2 Background

In this section, we give a brief introduction to the three-dimensional representation of the transmission function of crystalline materials, which is also commonly used in the TEM nomenclature.

**Scattering Matrix** The derivation of the scattering matrix in TEM highly depends on the theory of dynamical electron scattering in crystals. Starting from the non-relativistic stationary Schrödinger equation, with relativistic corrections made by Dirac, and by neglecting the spin, the Klein-Gordon equation can be used to describe the scattering of relativistic electrons in TEM:

$$\Delta\Psi(\mathbf{r}) + 4\pi^2k_0^2\Psi(\mathbf{r}) = -\frac{8\pi^2me}{h^2}V(\mathbf{r})\Psi(\mathbf{r}), \quad (1)$$

where  $V$  is the electrostatic potential at three-dimensional real space coordinates  $\mathbf{r} = (x, y, z)^T$ ,  $m$  is the relativistic electron mass,  $h$  is the Planck constant,  $e$  is the elementary charge, and  $k_0$  is the relativistic wave number. Intuitively, the goal is to find proper wave functions  $\Psi$  that fulfill the Schrödinger equation, specifically to quantify the scattering processes in the crystal.

As discussed in [17, eq. 5.43], the strategy to solve the partial differential equation in (1) is by involving the expansion in the Fourier space, also called reciprocal space. Firstly, the potential is expanded into its Fourier series, as follows:

$$V(\mathbf{r}) = \sum_{\mathbf{h}} V_{\mathbf{h}} \exp(i2\pi\mathbf{h} \cdot \mathbf{r}),$$

where  $V_{\mathbf{h}}$  is the lattice potential in reciprocal space. Secondly, the Bloch wave is incorporated, given as

$$\Psi(\mathbf{r}) = c(\mathbf{r}) \exp(i2\pi\mathbf{k} \cdot \mathbf{r}) = \sum_{\mathbf{g}} c_{\mathbf{g}} \exp(i2\pi(\mathbf{k} + \mathbf{g}) \cdot \mathbf{r}),$$

where  $\mathbf{k}, \mathbf{g} \in \mathbb{R}^3$  are wave and reciprocal space vectors, respectively. Variable  $c_{\mathbf{g}}$  is the Bloch wave coefficient in reciprocal space. By rearranging this equation and writing the wave functions and potential in reciprocal space coordinates, we obtain the eigenvalue equation, the solution of which is the scattering matrix formulation. For a complete derivation, we refer the interested readers to the literature, for instance [17, 22, 23].

Equation (1) allows us to model the interaction of the input-wave function with the crystal as a multiplication with the scattering matrix  $\mathbf{S} \in \mathbb{C}^{N^2 \times N^2}$ . In other words, it describes the transmission function of the specimen. The scattering matrix  $\mathbf{S}$  can be decomposed by eigenvalue decomposition, i.e.,

$$\mathbf{S} := \mathbf{C}\mathbf{A}\mathbf{C}^{-1} \in \mathbb{C}^{N^2 \times N^2}, \quad (2)$$

where  $\mathbf{C}$  is a unitary matrix representing the eigenvector of the matrix and  $\mathbf{A}$  is a diagonal matrix representing the eigenvalues with the diagonal elements containing the specimen thickness  $T$ , given as

$$(\exp(2\pi i\gamma_1 T), \exp(2\pi i\gamma_2 T), \dots, \exp(2\pi i\gamma_{N^2} T)).$$

The elements of the eigenvector matrix  $\mathbf{C}$  are the Bloch wave Fourier coefficients and can be written as

$$\mathbf{C} = \begin{pmatrix} \vdots & \vdots & \vdots & \vdots & \vdots \\ c_{\mathbf{h}}^1 & c_{\mathbf{h}}^2 & \dots & c_{\mathbf{h}}^i & \dots \\ c_{\mathbf{g}}^1 & c_{\mathbf{g}}^2 & \dots & c_{\mathbf{g}}^i & \dots \\ c_{\mathbf{0}}^1 & c_{\mathbf{0}}^2 & \dots & c_{\mathbf{0}}^i & \dots \\ c_{-\mathbf{g}}^1 & c_{-\mathbf{g}}^2 & \dots & c_{-\mathbf{g}}^i & \dots \\ c_{-\mathbf{h}}^1 & c_{-\mathbf{h}}^2 & \dots & c_{-\mathbf{h}}^i & \dots \\ \vdots & \vdots & \vdots & \vdots & \vdots \end{pmatrix} \in \mathbb{C}^{N^2 \times N^2}, \quad (3)$$

where  $\mathbf{h} \in \mathbb{R}^3$  and  $\mathbf{g} \in \mathbb{R}^3$  represent the reciprocal lattice vectors.

The scattering matrix encodes the information of the structure matrix  $\mathbf{B} \in \mathbb{C}^{N^2 \times N^2}$  representing the electrostatic potential of the underlying crystal,

$$\mathbf{S} = \exp(i2\pi T\mathbf{B}).$$

Due to the nature of matrix exponentiation, both  $\mathbf{S}$  and  $\mathbf{B}$  share eigenvectors  $\mathbf{C}$ , and  $\gamma_j$ ,  $j \in [N^2]$  are the eigenvalues of  $\mathbf{B}$ . Moreover, the elements of matrix  $\mathbf{B}$  are given by

$$\mathbf{B} = \begin{pmatrix} \vdots & \vdots & \vdots & \vdots & \vdots & \vdots & \vdots \\ \dots & s_{\mathbf{h}} & V_{\mathbf{h}-\mathbf{g}} & V_{\mathbf{h}} & V_{\mathbf{h}+\mathbf{g}} & V_{2\mathbf{h}} & \dots \\ \dots & V_{\mathbf{g}-\mathbf{h}} & s_{\mathbf{g}} & V_{\mathbf{g}} & V_{2\mathbf{g}} & V_{\mathbf{h}+\mathbf{g}} & \dots \\ \dots & V_{-\mathbf{h}} & V_{-\mathbf{g}} & s_{\mathbf{0}} & V_{\mathbf{g}} & V_{\mathbf{h}} & \dots \\ \dots & V_{-\mathbf{g}-\mathbf{h}} & V_{-2\mathbf{g}} & V_{-\mathbf{g}} & s_{-\mathbf{g}} & V_{-\mathbf{g}+\mathbf{h}} & \dots \\ \dots & V_{-2\mathbf{h}} & V_{-\mathbf{h}-\mathbf{g}} & V_{-\mathbf{h}} & V_{-\mathbf{h}+\mathbf{g}} & s_{-\mathbf{h}} & \dots \\ \vdots & \vdots & \vdots & \vdots & \vdots & \vdots & \vdots \end{pmatrix} \in \mathbb{C}^{N^2 \times N^2}, \quad (4)$$

where the diagonal and off-diagonal elements represent the excitation error and, respectively, potential in reciprocal space. In Figure 1(b) the relation between the crystal and the scattering matrix is illustrated.

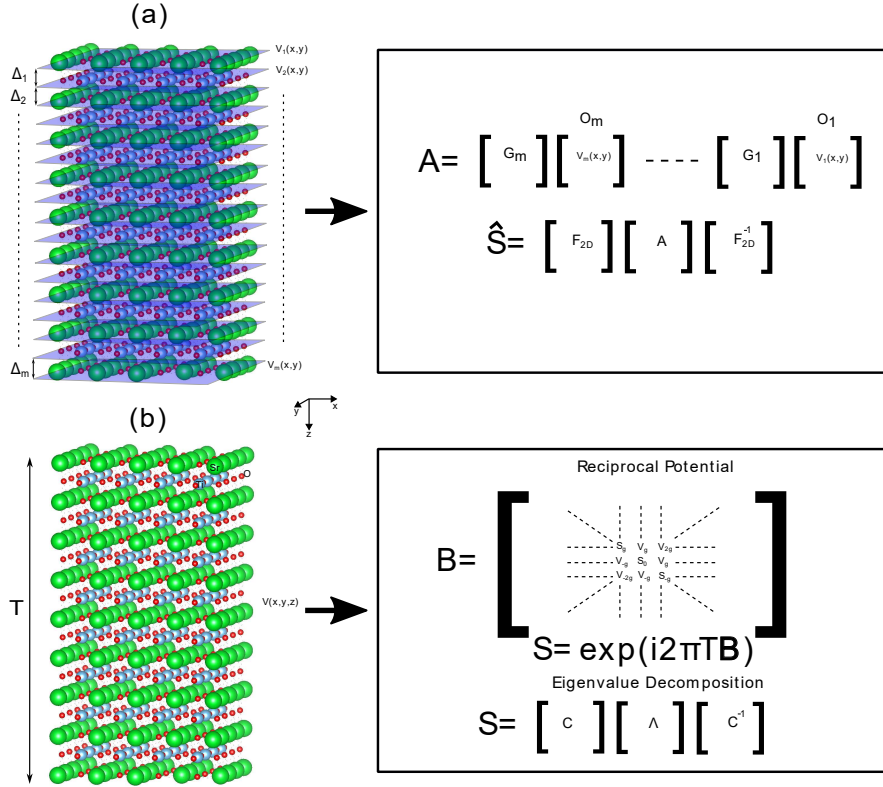


Figure 1: Visualization of a  $\text{SrTiO}_3$  crystal and the relation of its atomic structure to (a) the mathematical notation of the multislice method and (b) the Bloch wave formulation, as well as the construction of the respective matrices  $\hat{\mathbf{S}}$  and  $\mathbf{S}$ . The Bloch wave method incorporates all lattice potentials  $V(x, y, z)$  within the specimen of thickness  $T$  in a single matrix entity, while with the multislice method the calculation is performed on projected lattice potentials  $V_m(x, y)$  of many thin slices with distance  $\Delta_m$  in several matrices  $\mathbf{O}_m$ .

**Transmission Matrix** Apart from the Bloch wave-derived scattering matrix, the multislice method is frequently used to model the interaction between an incident electron wave and the crystal potential. Instead of directly deriving an analytical solution as in the Bloch wave approach, the transmission function can be constructed using multiple infinitely thin (sub-)specimens i.e. slices, separated by free space.

More precisely, let  $V(x, y, z)$  denote the potential energy of the crystal and set the projected potential of the  $m$ -th slice as  $V_m(x, y) = \int_{z_m}^{z_{m+1}} V(x, y, z) dz$ . Then, the transmission matrix corresponding to a crystal with  $M$  slices is given by

$$\mathbf{A} = \prod_{m=1}^M \mathbf{G}_m \mathbf{O}_m,$$

where  $\mathbf{O}_m \in \mathbb{C}^{N^2 \times N^2}$  is the diagonal matrix representing the potential of the slice with elements

$$(\mathbf{O}_m)_{x+N(y-1), x+N(y-1)} = \exp(i\sigma V_m(x, y)) \text{ for } x, y \in [N], \quad (5)$$

with the interaction constant  $\sigma$  for relativistic correction. The matrix  $\mathbf{G}_m$  is the Fresnel propagator in free space defined by

$$\mathbf{G}_m := \mathbf{F}_{2D}^{-1} \mathbf{D}_m \mathbf{F}_{2D} \in \mathbb{C}^{N^2 \times N^2}, \quad m \in [M], \quad (6)$$

where  $\mathbf{F}_{2D}, \mathbf{F}_{2D}^{-1} \in \mathbb{C}^{N^2 \times N^2}$  are two-dimensional unitary Fourier and inverse Fourier matrices, respectively. The matrix  $\mathbf{D}_m \in \mathbb{C}^{N^2 \times N^2}$  is a diagonal matrix where each diagonal element can be written as

$$(\mathbf{D}_m)_{x+N(y-1), x+N(y-1)} := \exp(-\pi i \Delta_m \lambda Q_{xy}) \text{ for } x, y \in [N], \quad (7)$$

where  $Q_{xy} = (q_y^2 + q_x^2) + 2 \left( q_x \frac{\sin \theta_x}{\lambda} + q_y \frac{\sin \theta_y}{\lambda} \right)$ . The parameters  $q_y, q_x$  are the discrete grid in reciprocal space and hence represent spatial frequencies,  $\Delta_m$  is the distance of the wave propagation with parameters  $\Delta_m = z_{m+1} - z_m$ , and  $\theta_x, \theta_y$  are the two-dimensional tilt angles, describing the direction of the incoming wave. An illustration visualizing the multislice method is shown in Figure 1(a).

Unlike the scattering matrix, which is defined in reciprocal space, the matrix  $\mathbf{A}$  as reformulation of the multislice method is set in real space. Thus, we instead consider the transmission matrix:

$$\hat{\mathbf{S}} = \mathbf{F}_{2D} \mathbf{A} \mathbf{F}_{2D}^{-1}. \quad (8)$$

The right multiplication transforms the input wave from reciprocal space back into real space, and the left multiplication transforms the exit wave into reciprocal space to model the diffraction pattern in the back focal plane of a TEM.

As highlighted in [2,17], the multislice method serves as an alternative to the Bloch wave formulation, making the transmission matrix  $\hat{\mathbf{S}}$  which we have derived from the multislice method an approximate solution to the Schrödinger equation (1). The main advantage that this reformulation offers is that the atomic structure of a crystalline object can now be represented independently by the transmission matrix  $\hat{\mathbf{S}}$ , without being influenced by the electron probe, which is not the case in the classical multislice model. In addition, compared to the Bloch wave formulation, which depends on the computation complexity of eigenvalue decomposition to construct the scattering matrix, the multislice method enables more efficient computation of the scattering processes by leveraging the fast Fourier transform. We also provide analysis on the computational complexity to construct both transmission and scattering matrix in the numerical section.

### 3 Eigenstructure Analysis and its Applications

In the following, we will discuss the equivalence of the transmission matrix  $\hat{\mathbf{S}}$  in (8) and scattering matrix  $\mathbf{S}$  in (2) in terms of their eigenstructure. We will also draw a connection to estimate the mean inner potential from the transmission matrix.

First, we investigate the eigenvalue decomposition of  $\hat{\mathbf{S}} = \mathbf{F}_{2D} \mathbf{A} \mathbf{F}_{2D}^{-1}$ . By construction, we have

$$\mathbf{A} = \prod_{m=1}^M \mathbf{G}_m \mathbf{O}_m = \prod_{m=1}^M \mathbf{F}_{2D}^{-1} \mathbf{D}_m \mathbf{F}_{2D} \mathbf{O}_m.$$

Matrices  $\mathbf{D}_m$  and  $\mathbf{O}_m$  are both diagonal with unit modulus entries, and are therefore unitary. Fourier transforms are also unitary and, consequently,  $\mathbf{A}$  and  $\hat{\mathbf{S}}$  are unitary being products of unitary matrices. Hence, this also implies that both are normal matrices, i.e., they satisfy  $\mathbf{A}^H \mathbf{A} = \mathbf{A} \mathbf{A}^H = \mathbf{I}$ . As a result,  $\mathbf{A}$  admits eigenvalue decomposition  $\mathbf{A} = \mathbf{W} \mathbf{V} \mathbf{W}^{-1}$  with a unitary matrix  $\mathbf{W}$ , which columns are the eigenvectors of  $\mathbf{A}$ , and with the diagonal matrix  $\mathbf{V}$  with eigenvalues of  $\hat{\mathbf{S}}$  on its diagonal. Since  $\mathbf{A}$  is unitary, the eigenvalues are of unit modulus and can be written in terms of a complex exponential,  $\lambda_k(\mathbf{A}) = \exp(i2\pi\theta_k)$ , where  $\theta_k \in [0, 1]$  for  $k \in [N^2]$ .

*Remark 1.* Suppose we have a specific case where each slice  $\mathbf{O}$  has an equidistant thickness  $\Delta$  of the dimension of the specimen unit cell to generate the projected potential, i.e.,  $\Delta = \Delta_1 = \Delta_2 = \dots = \Delta_M$  and slice  $\mathbf{O} = \mathbf{O}_1 = \mathbf{O}_2 = \dots = \mathbf{O}_M$ . Hence, we have the transmission function matrix as matrix power  $\mathbf{A} = (\mathbf{G}\mathbf{O})^M$  and the eigenvalues can be written as  $\lambda_k(\mathbf{A}) = \exp(i2\pi M\theta_k)$  for  $k \in [N^2]$  and  $\theta_k \in [0, 1]$ . It should be noted that, since the two-dimensional Fourier matrices  $\mathbf{F}_{2D}, \mathbf{F}_{2D}^{-1}$  are unitary, the structure of the transmission matrix  $\hat{\mathbf{S}} = \mathbf{F}_{2D} \mathbf{A} \mathbf{F}_{2D}^{-1}$  does not change.

Understanding the eigenstructure of scattering and transmission matrices is crucial for analyzing their similarity. In the subsequent sections, we will discuss the conditions under which the matrices are equal.

**Characterizing Similarity** To quantify any differences, the scattering and the transmission matrix are compared using the Frobenius norm within a metric space. This norm acts as a distance metric, enabling the assessment of the accuracy and consistency between both matrices, as detailed below:

$$\begin{aligned}\|\mathbf{S} - \hat{\mathbf{S}}\|_F^2 &= \text{trace} \left( (\mathbf{S} - \hat{\mathbf{S}})^H (\mathbf{S} - \hat{\mathbf{S}}) \right) \\ &= \text{trace} (\mathbf{S}^H \mathbf{S}) + \text{trace} (\hat{\mathbf{S}}^H \hat{\mathbf{S}}) - \text{trace} (\mathbf{S}^H \hat{\mathbf{S}}) - \text{trace} (\hat{\mathbf{S}}^H \mathbf{S}) \\ &\stackrel{(a)}{=} 2 \text{trace} (\mathbf{I}) - \text{trace} (\mathbf{C} \Lambda^H \mathbf{C}^{-1} \mathbf{F}_{2D} \mathbf{A} \mathbf{F}_{2D}^{-1}) - \text{trace} (\mathbf{F}_{2D} \mathbf{A}^H \mathbf{F}_{2D}^{-1} \mathbf{C} \Lambda \mathbf{C}^{-1}),\end{aligned}$$

where the equality in (a) is derived from the unitary property of both scattering and transmission matrix. The difference between scattering matrix  $\mathbf{S} = \mathbf{C} \Lambda \mathbf{C}^{-1}$  and transmission matrix  $\hat{\mathbf{S}} = \mathbf{F}_{2D} \mathbf{A} \mathbf{F}_{2D}^{-1}$  highly depends on the trace of their product. In case both matrices are equal, their difference should be zero. This condition can be directly derived by

$$\mathbf{C} \Lambda^H \mathbf{C}^{-1} \mathbf{F}_{2D} \mathbf{A} \mathbf{F}_{2D}^{-1} = \mathbf{F}_{2D} \mathbf{A}^H \mathbf{F}_{2D}^{-1} \mathbf{C} \Lambda \mathbf{C}^{-1} = \mathbf{I}.$$

Suppose we perform an eigenvalue decomposition on the matrix  $\mathbf{A}$ , as follows

$$\mathbf{F}_{2D} \mathbf{A} \mathbf{F}_{2D}^{-1} = \mathbf{F}_{2D} \mathbf{W} \mathbf{V} \mathbf{W}^{-1} \mathbf{F}_{2D}^{-1},$$

where the diagonal matrix  $\mathbf{V}$  and matrix  $\mathbf{W}$  are the eigenvalues and eigenvectors of matrix  $\mathbf{A}$ , respectively. Since the eigenvectors  $\mathbf{C}$  of the scattering matrix are the Fourier coefficients of the Bloch wave, one possible solution is that the eigenvector  $\mathbf{W}$  is the Bloch wave itself. This relation holds, because each column element of the eigenvector matrix  $\mathbf{C}$  is a Fourier coefficient of the Bloch wave. Therefore, we can write  $\mathbf{C} = \mathbf{F}_{2D} \mathbf{W}$ , and the equation can be written as

$$\begin{aligned}\text{trace} (\mathbf{C} \Lambda^H \mathbf{C}^{-1} \mathbf{F}_{2D} \mathbf{W} \mathbf{V} \mathbf{W}^{-1} \mathbf{F}_{2D}^{-1}) &= \text{trace} (\mathbf{C} \Lambda^H \mathbf{V} \mathbf{C}^{-1}) \\ &\stackrel{(b)}{=} \text{trace} (\Lambda^H \mathbf{V}).\end{aligned}$$

The equality (b) is due to the fact that the trace is invariant under circular shifts, namely

$$\text{trace} (\mathbf{C} \Lambda^H \mathbf{V} \mathbf{C}^{-1}) = \text{trace} (\Lambda^H \mathbf{V} \mathbf{C}^{-1} \mathbf{C}).$$

As a result, the difference between both matrices can be expressed as

$$\begin{aligned}\|\mathbf{S} - \hat{\mathbf{S}}\|_F^2 &= 2N^2 - \text{trace} (\Lambda^H \mathbf{V}) - \text{trace} (\Lambda \mathbf{V}^H), \\ &\stackrel{(c)}{=} 2N^2 - \left( \sum_{k=1}^{N^2} \exp(i2\pi(\gamma_k T - \theta_k)) + \sum_{k=1}^{N^2} \exp(-i2\pi(\gamma_k T - \theta_k)) \right) \\ &\stackrel{(d)}{=} 2N^2 - 2 \sum_{k=1}^{N^2} \cos(2\pi(\gamma_k T - \theta_k)).\end{aligned}\tag{9}$$

The equality (c) is derived from the fact that the eigenvalue of matrix  $\mathbf{S}$  is  $\exp(i2\pi\gamma_k T)$  for  $k \in [N^2]$  and that matrix  $\mathbf{A}$  is a unitary matrix with modulus eigenvalues of the form  $\exp(i2\pi\theta_k)$  for  $k \in [N^2]$ . Therefore, the equivalence between the two matrices in terms of the Frobenius norm holds as long as the following conditions are satisfied:

- Eigenvectors  $\mathbf{C}$  of scattering matrix  $\mathbf{S}$  and eigenvectors  $\mathbf{W}$  of matrix  $\mathbf{A}$  are related in terms of a two-dimensional Fourier matrix, namely  $\mathbf{C} = \mathbf{F}_{2D} \mathbf{W}$ .
- The angles of both the eigenvalue matrix  $\Lambda$ , obtained from scattering matrix  $\mathbf{S}$ , and the eigenvalue matrix  $\mathbf{V}$ , obtained from matrix  $\mathbf{A}$ , differ by up to modulo  $2\pi n$  for integers  $n = \gamma_k T - \theta_k$ .

*Remark 2.* Matrix  $\mathbf{A}$  can also be approximated by applying two-dimensional Fourier transform and inverse Fourier transform to the scattering matrix, i.e.,  $\mathbf{A} \approx \mathbf{F}_{2D}^{-1} \mathbf{S} \mathbf{F}_{2D}$ . This is true, because the eigenvector of the scattering matrix  $\mathbf{S}$  is the Fourier coefficient of the Bloch wave, as discussed in (3). Consequently, the same total projected potential can be obtained from both matrix  $\mathbf{A}$  and  $\mathbf{F}_{2D}^{-1} \mathbf{S} \mathbf{F}_{2D}$ . We will show numerically in Section 5, that both matrices produce a very similar projected potential.

**Determinant and Mean Inner Potential** Apart from characterizing similarity, we can also estimate the mean inner potential (MIP) from the eigenstructure in terms of the determinant. The determinant of the scattering matrix  $\mathbf{S}$  is well-known and can be derived as

$$\det(\mathbf{S}) = \prod_{j=1}^{N^2} \exp(2\pi i \gamma_j T) = \exp(2\pi i T \gamma_{total}),$$

where  $T$  is the thickness parameter and  $\gamma_{total} = \sum_{j=1}^{N^2} \gamma_j$ . For the transmission matrix  $\hat{\mathbf{S}}$ , the determinant can be derived as follows

$$\begin{aligned} \det(\mathbf{F}_{2D} \mathbf{A} \mathbf{F}_{2D}^{-1}) &= \det(\mathbf{F}_{2D}) \det(\mathbf{A}) \det(\mathbf{F}_{2D}^{-1}) = \det\left(\prod_{m=1}^M \mathbf{G}_m \mathbf{O}_m\right) \\ &= \det(\mathbf{G}_1 \mathbf{O}_1) \det(\mathbf{G}_2 \mathbf{O}_2) \dots \det(\mathbf{G}_M \mathbf{O}_M). \end{aligned} \quad (10)$$

The equality holds because  $\det(\mathbf{F}_{2D}^{-1}) = 1/\det(\mathbf{F}_{2D})$  and the determinant of a matrix product is equal to the product of the determinants of the individual factors. Let us further expand the determinant for each slice  $\mathbf{O}_m$  including the Fresnel matrix  $\mathbf{G}_m$  for  $m \in [M]$ ,

$$\begin{aligned} \det(\mathbf{G}_m \mathbf{O}_m) &= \det(\mathbf{F}_{2D}^{-1} \mathbf{D}_m \mathbf{F}_{2D}) \det(\mathbf{O}_m) \\ &\stackrel{(a)}{=} \exp\left(-\pi i \Delta_m \lambda \sum_{x=1}^N \sum_{y=1}^N Q_{xy}\right) \exp\left(i\sigma \sum_{x=1}^N \sum_{y=1}^N V_m(x, y)\right) \\ &\stackrel{(b)}{=} \exp\left(-i \left(\pi \Delta_m \lambda \sum_{x=1}^N \sum_{y=1}^N Q_{xy} - \sigma \sum_{x=1}^N \sum_{y=1}^N V_m(x, y)\right)\right) \\ &\stackrel{(c)}{=} \exp(-i(\pi \Delta_m \lambda Q - \sigma V_m)) \end{aligned} \quad (11)$$

Since  $\det(\mathbf{F}_{2D}^{-1}) = 1/\det(\mathbf{F}_{2D})$ , we have the determinants of the diagonal matrices  $\mathbf{D}_m$  and  $\mathbf{O}_m$ , yielding the product of the exponential functions in their diagonal elements, as shown in (b). Equality (c), (d) are derived by combining the two exponential functions and substituting the parameters  $Q = \sum_{x=1}^N \sum_{y=1}^N Q_{xy}$  and  $V_m = \sum_{x=1}^N \sum_{y=1}^N V_m(x, y)$ . The parameter  $Q$  is the sum over the whole reciprocal space, including the tilt angle parameters given in (7), and  $V_m$  is the sum of the discrete projected potentials for each slice. Hence, the product of  $M$  slices can be written as

$$\begin{aligned} \prod_{m=1}^M \det(\mathbf{G}_m \mathbf{O}_m) &\stackrel{(e)}{=} \prod_{m=1}^M \exp(-i(\pi \Delta_m \lambda Q - \sigma V_m)) \\ &\stackrel{(f)}{=} \exp\left(-i \left(\pi \lambda Q \sum_{m=1}^M \Delta_m - \sigma \sum_{m=1}^M V_m\right)\right) \\ &\stackrel{(g)}{=} \exp(-i(\pi \lambda Q T - \sigma V_{total})). \end{aligned} \quad (12)$$

The equality (e) follows from combining (10) with (11). As a consequence and as shown in (f) and (g), we can substitute  $T = \sum_{m=1}^M \Delta_m$ , which is the total thickness of the crystal, and substitute the total projected potential  $V_{total} = \sum_{m=1}^M V_m$ , which is the summation of all projected potentials in all slices given in (5) for the thickness  $T$ .

*Remark 3.* It can be seen that  $V_{total}$  is the total of all projected potentials in the crystal volume in the discrete case, namely the summation is taken for all slices and all discrete grids of the potential

$$V_{total} = \sum_{m=1}^M \sum_{x=1}^N \sum_{y=1}^N V_m(x, y) = \sum_{m=1}^M \sum_{x=1}^N \sum_{y=1}^N \int_{z_m}^{z_{m+1}} V(x, y, z) dz.$$

Generalizing for the continuous case leads to

$$V_{total} = \sum_{m=1}^M \int_{z_m}^{z_{m+1}} \int_y \int_x V(x, y, z) dx dy dz = \int_z \int_y \int_x V(x, y, z) dx dy dz.$$

This result is a direct implication of calculating the determinant as a metric to measure the volume of a parallelepiped, defined by the structure of the lattice vectors. Similarly, the quantity  $TQ$  is the volume in reciprocal space for the discrete case

$$TQ = \sum_{m=1}^M \Delta_m \sum_{x=1}^N \sum_{y=1}^N Q_{xy} = \sum_{m=1}^M \Delta_m \left[ \sum_{x=1}^N \sum_{y=1}^N (q_y^2 + q_x^2) + 2 \left( q_x \frac{\sin \theta_x}{\lambda} + q_y \frac{\sin \theta_y}{\lambda} \right) \right],$$

where in the continuous case we can write

$$QT = \int_0^T \int_{q_y} \int_{q_x} (q_y^2 + q_x^2) + 2 \left( q_x \frac{\sin \theta_x}{\lambda} + q_y \frac{\sin \theta_y}{\lambda} \right) dq_x dq_y dz.$$

If we define a constant slice thickness of the unit cell height,  $\Delta_m = \Delta$ , and have a similar projected potential within each slice  $m \in [M]$ , we have  $T = M\Delta$  and  $V_{total} = MV$  for each slice potential  $V$ .

The structure of the transmission matrix allows us to estimate the MIP from its determinant. The MIP represents the inner structure of a crystal and is calculated by taking the average of the Coulomb potential over a unit cell, given as

$$V_0 = \frac{1}{\Omega} \int_{\Omega} V(\mathbf{r}) d\mathbf{r}.$$

Here the  $\Omega$  is the considered volume of the crystal [1]. The MIP affects the interaction between electrons in a material; it has been studied and estimated in numerous works [24–38].

Taking the logarithm of the determinant of the transmission matrix  $\hat{S} = \mathbf{F}_{2D} \mathbf{A} \mathbf{F}_{2D}^{-1}$  yields a direct estimation of the total potential inside the material

$$\log \det (\mathbf{F}_{2D} \mathbf{A} \mathbf{F}_{2D}^{-1}) = -i (\pi \lambda QT - \sigma V_{total}) + 2\pi n, \quad (13)$$

where  $2\pi n$  with an integer  $n$  results from the periodicity of the complex exponent. Hence, we can write the total potential as

$$V_{total} = \frac{1}{\sigma} (\pi \lambda QT - i \log \det (\mathbf{F}_{2D} \mathbf{A} \mathbf{F}_{2D}^{-1})) + 2\pi n. \quad (14)$$

Scaling with the volume dimension we measure, we can estimate the MIP of crystalline materials directly. It should be noted that, unlike for the case of a thin specimen, for a thick specimen the contributing factor such as Fresnel propagation should be removed, in order to retrieve a pure MIP. The estimation of the MIP from the determinant for simulated and experimental data is discussed in Section 5.

## 4 Simulated and Experimental Datasets

In the following section, we compare Bloch wave and multislice methods using simulated datasets of three crystalline materials: gallium arsenide (GaAs), a binary compound semiconductor, strontium titanate (SrTiO<sub>3</sub>), a ternary oxide, and gold (Au), a single element crystal. These materials differ in terms of total number and type (atomic number  $Z$ ) of elements, and cubic unit cell dimension. Representations of the unit cell of each material in projection along the  $[001]$  crystallographic direction and in perspective view are shown in Figure 2.

Table 1: Simulation parameters used to generate scattering and transmission matrix with both the Bloch wave formulation and the multislice method, respectively. Structure data for GaAs [39], SrTiO<sub>3</sub> [40] and Au [39] was used. For the simulated data, each slice represents the projected potential of all atoms within one atomic layer. The Fresnel distance is the distance which the projected potential of a single slice is required to be propagated and corresponds to the lattice spacing along  $[001]$ .

Parameters	GaAs ( $\mathbf{F}\bar{4}3\mathbf{m}$ )	SrTiO <sub>3</sub> ( $\mathbf{Pm}\bar{3}\mathbf{m}$ )	Au ( $\mathbf{Fm}\bar{3}\mathbf{m}$ )
Unit cell (a,b,c) (Å)	(5.6533, 5.6533, 5.6533)	(3.905, 3.905, 3.905)	(4.08, 4.08, 4.08)
Unit cell ( $\alpha, \beta, \gamma$ ) (°)	(90, 90, 90)	(90, 90, 90)	(90, 90, 90)
Pixel size (Å)	(0.1739, 0.1739)	(0.1201, 0.1201)	(0.1255, 0.1255)
Fresnel distance (Å)	(1.413325, 1.413325)	(1.9525, 1.9525)	(2.04, 2.04)
Accel. voltage (keV)	300	300	300

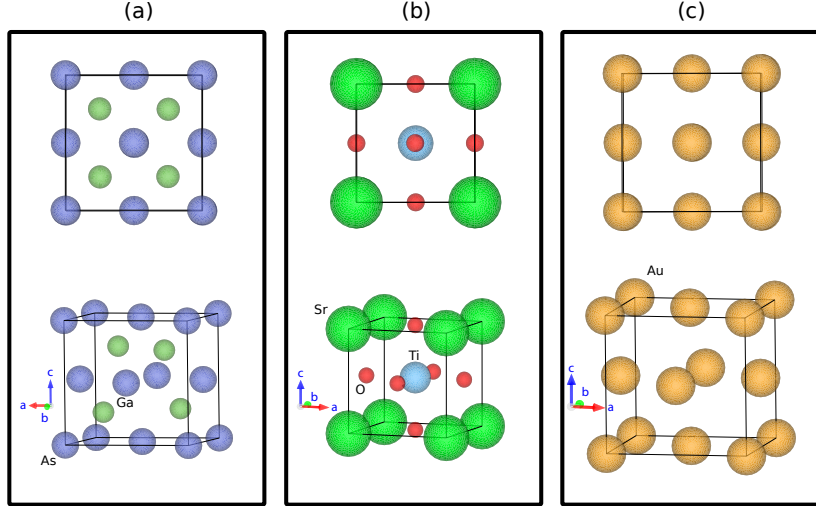


Figure 2: Unit cells of (a) gallium arsenide (GaAs), (b) strontium titanate (SrTiO<sub>3</sub>) and (c) gold (Au), shown in [001] projection (top row) and 3D representation (bottom row), of crystals used to generate the scattering and transmission matrix

The parameters used to generate the simulated datasets are summarized in Table 1, outlining crucial characteristics such as unit cell dimensions, pixel size, and Fresnel distance for each material. These parameters serve as inputs for the simulation of the electrostatic potentials and the generation of structure matrices. The parameters as well as the implementation of the multislice and Bloch wave methods to generate transmission and scattering matrices were adopted from [21].

For the experimental process, 2H-MoS<sub>2</sub> sheets were exfoliated from a bulk crystal using a polydimethylsiloxane elastomer film placed on a glass slide and subsequently transferred onto a holey silicon nitride membrane for TEM analysis. The experimental data for MoS<sub>2</sub> was gathered using a probe-corrected Hitachi HF5000 field emission microscope in scanning TEM mode (STEM), operating at an acceleration voltage of 200 keV with a beam current of approximately 7.4 pA. The intensities of the diffraction patterns were recorded with a Medipix3 Merlin4EM camera, with a resolution of 256 × 256 pixels. The distance between adjacent scan points was set to 26.5 pm in both the horizontal (x) and vertical (y) directions. Each diffraction pattern was acquired within 0.5 ms, and the data collection employed a 6-bit dynamic range.

Table 2: Experimental STEM data acquisition parameters for MoS<sub>2</sub>

Parameters	Data
Detector	Merlin Medipix3
Dimension (pixel)	128, 128, 256, 256
Accel. voltage (keV)	200
Scan rotation	176°
Semiconv. angle	32 mrad
Real space pixel size	0.26 Å

## 5 Numerical Experiments

In this section, we calculate the eigenstructure of the scattering and the transmission matrix, derived from Bloch waves and multislice formulation, respectively. We also show the distribution of eigenvalues as well as the projected potentials that result from both matrices. Additionally, we draw the connection to how to estimate the mean inner potential of a crystal from the determinant of the transmission matrix.

**Diffraction patterns.** First, we evaluate the diffraction patterns as a function of the specimen thickness for all three materials. The common approach to compare both matrix formulations would be the evaluation of the specimen exit wave as well as its intensity. For the evaluation of the Bragg diffraction,

the product of scattering i.e. transmission matrix with the illuminating plane-wave is performed. The amplitude of the computed Bragg diffraction patterns of the three specimens in  $[001]$ -orientation is shown in Figure 3. The results for both scattering and transmission matrix look very similar for each

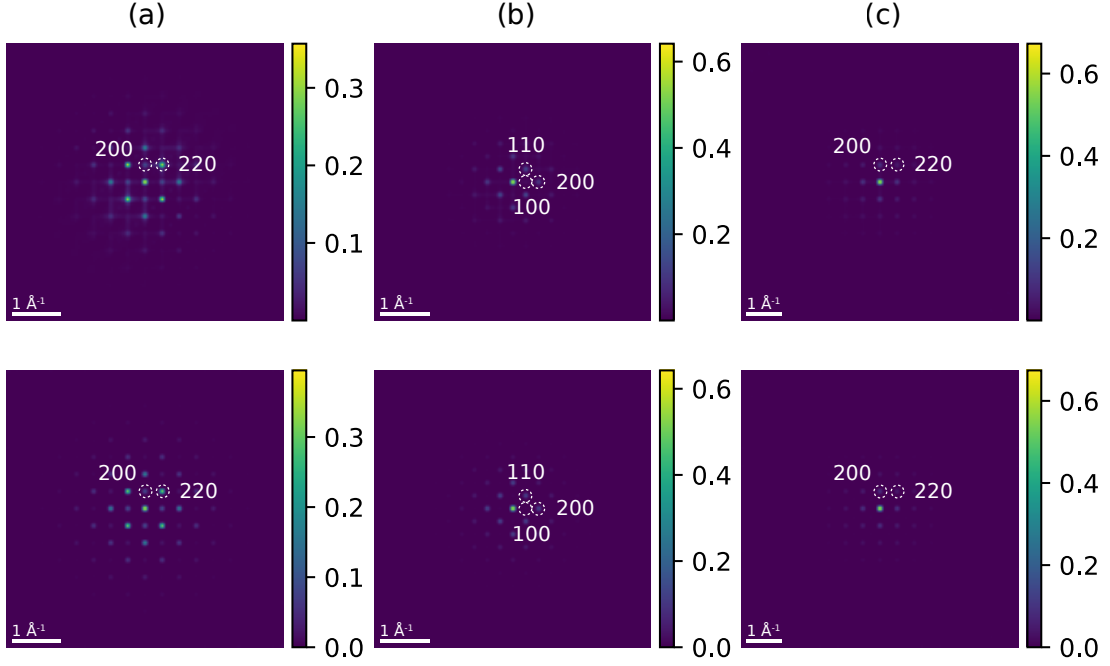


Figure 3: Diffraction patterns along the  $[001]$  zone axis calculated using the transmission matrix (top row) and the scattering matrix (bottom row) for (a) GaAs with simulated thickness  $175.2523 \text{ \AA}$ , (b)  $\text{SrTiO}_3$  with simulated thickness  $126.48 \text{ \AA}$ , (c) Au with simulated thickness  $121.055 \text{ \AA}$ .

specimen, indicating that any inherent differences are only marginal. To go into more detail, we evalu-

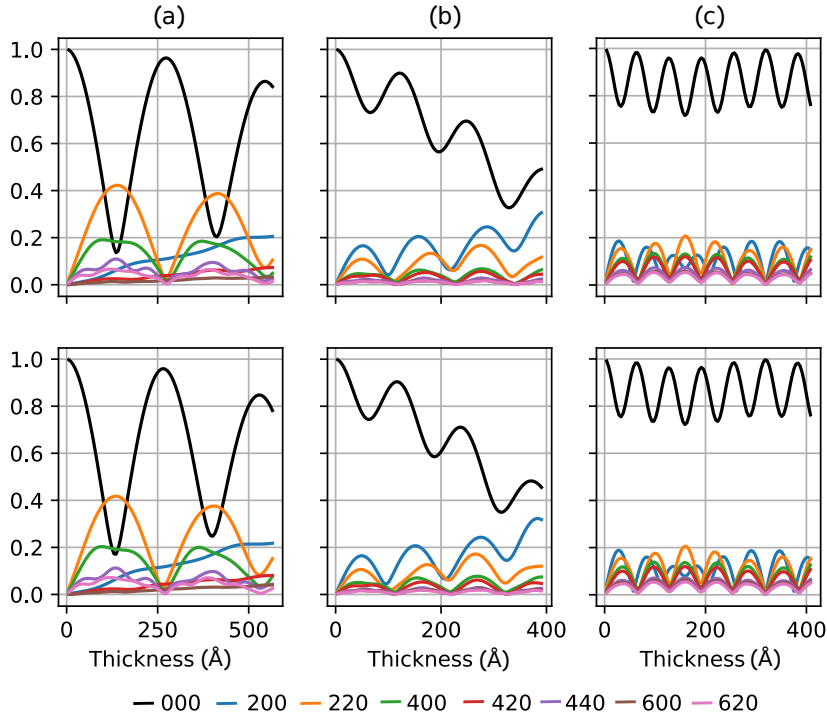


Figure 4: Bragg beam amplitude as a function of specimen thickness, calculated using the transmission matrix (top row) and the scattering matrix (bottom row) for (a) GaAs, (b)  $\text{SrTiO}_3$ , and (c) Au.

ated the propagation of several diffracted beams with increasing crystal thickness in order to compare

their resulting amplitudes between the scattering matrix and transmission matrix. This observation measures the similarity of both matrices in terms of intensity i.e. amplitude of the exit wave at plane-wave illumination, and is shown in Figure 4. When propagating through the crystal, the transmitted and the diffracted beams exhibit alternating amplitudes picturing the Pendellösung effect. Our computed intensities using the scattering and transmission matrix are in good agreement, confirming our previous evaluation of the diffraction patterns. However, slight differences are to be expected, e.g. a small shift of maxima and minima in Figure 4(a, b), as we compare two different approaches.

**Eigenstructure Evaluation.** A much more precise assessment of the similarity of transmission and scattering matrix can be achieved by analyzing their eigenstructure, such as eigenvalues and eigenvectors. Since both are unitary matrices and have eigenvalues with unit modulus, as discussed in Section 3, the comparison in terms of amplitude yields no differences. Therefore, we focus on evaluating the phase of the eigenvalues, as presented in Figure 5. The eigenvalues are sorted by index with the maximum index being the total dimension of the scattering and transmission matrix. Our comparison of the phase shows

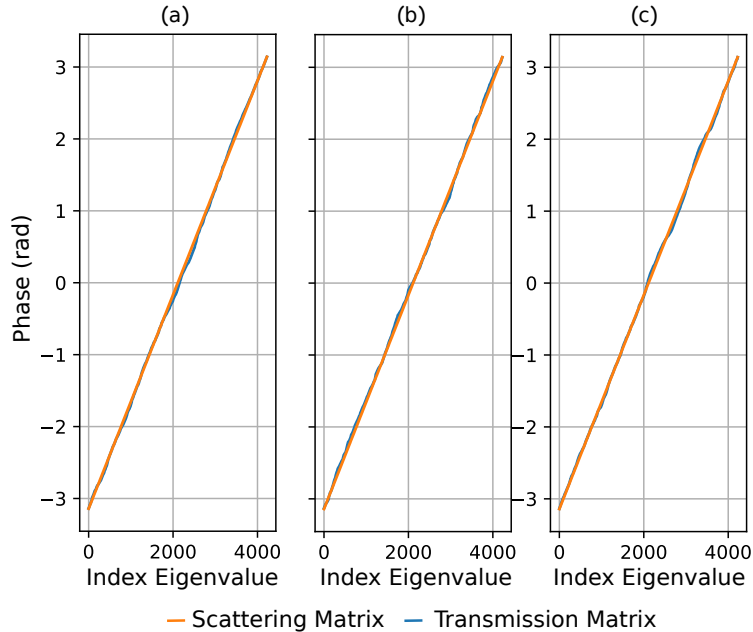


Figure 5: Phase distribution of eigenvalues from both transmission and scattering matrix for (a) GaAs with thickness 169.6 Å and a standard deviation (SD) of 0.037 rad, (b) SrTiO<sub>3</sub> with thickness 78.1 Å and SD = 0.034 rad, (c) Au with thickness 102 Å and SD = 0.035 rad.

a very similar result for both methods and all evaluated datasets. While with the scattering matrix the increase of the phase is perfectly linear, the phase obtained using the transmission matrix shows small deviations of up to 64 mrad and appear to be independent of index and matrix size.

**Projected Potential.** Apart from the phase distribution of the determinant of scattering and transmission matrix, we have discussed the similarity of both matrices in terms of their eigenvectors and eigenvalue, as presented in (9). The eigenvector of transmission matrix  $\hat{\mathbf{S}} = \mathbf{F}_{2D}\mathbf{A}\mathbf{F}_{2D}^{-1}$  should therefore be equal to the Fourier coefficients of the Bloch wave, and consequently, we can directly estimate the projected potential of a crystal from the scattering matrix by multiplying with the two-dimensional Fourier and inverse Fourier matrices. Mathematically, we can write  $\mathbf{A} \approx \mathbf{F}_{2D}^{-1}\mathbf{S}\mathbf{F}_{2D}$ . Hence, from this approximation, we can directly obtain matrix  $\mathbf{A}$  from the scattering matrix, which can be used to retrieve the two-dimensional projected potential, as given in Figure 6. It can be seen that, for all crystals considered, we can retrieve a very similar projected potential, using either the scattering or the transmission matrix.

As an example for a practical application, we calculated the projected potential using the transmission matrix for a reconstruction from experimental STEM diffraction pattern data of MoS<sub>2</sub>. Here, we leverage the sparse matrix decomposition algorithm discussed in [15]. The resulting projected potential is shown in Figure 7, where the hexagonal atomic arrangement of MoS<sub>2</sub> is well resolved. Experimental parameters are given in Table 2.

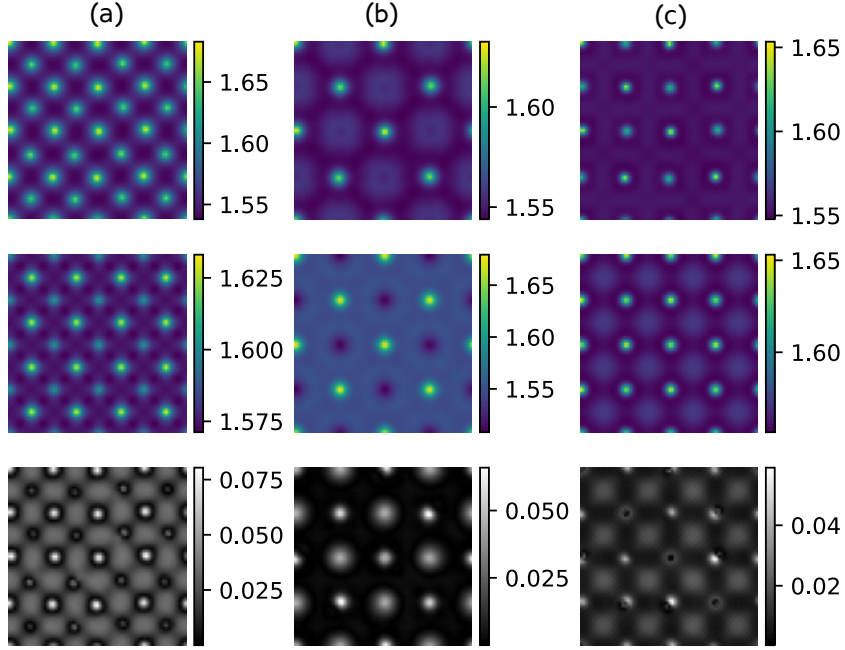


Figure 6: Projected potential of  $2 \times 2$  unit cells in  $[001]$  zone axis of (a) GaAs with thickness  $169.6 \text{ \AA}$  (30 unit cells), (b)  $\text{SrTiO}_3$  with thickness  $78.1 \text{ \AA}$  (20 unit cells), (c) Au with thickness  $102 \text{ \AA}$  (25 unit cells). The top row is calculated with the transmission matrix and the middle row with the scattering matrix. Their absolute difference is shown in the bottom row.

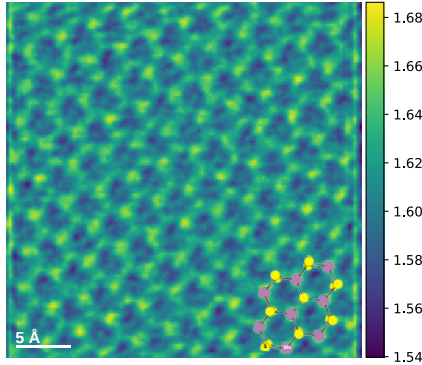


Figure 7: Projected potential of a  $\text{MoS}_2$  multilayer oriented close to  $[0001]$  zone axis. A schematic atomic model of  $\text{MoS}_2$  is superimposed for reference. The potential was calculated from an experimental STEM dataset reconstructed with the method in [15]. The output is presented as is; no aberration or focus correction was applied in the reconstruction.

**Mean Inner Potential.** The estimation of the MIP  $V_0$  from the determinant in (14) is shown in Table 3. The comparison with existing results from density functional theory (DFT) as well as experimental data is also provided. In general, by using the determinant up to modulo  $2\pi n$  for integer  $n$ , we are able to estimate the MIP of crystalline materials for both simulated and experimental data in very good agreement with tabulated values.

**Computational Complexity** We compare the computational complexity for the construction of both  $N^2 \times N^2$  transmission and scattering matrices. The construction of the scattering matrix depends on the computation of eigenvalue decomposition of the structure matrix, which requires  $\mathcal{O}(N^6)$ . For the transmission matrix, we perform the sequential matrix product of Fresnel matrices  $\mathbf{G}_m$  and diagonal potential matrices  $\mathbf{O}_m$ . We start with the first potential matrix  $\mathbf{O}_1$ . The product  $\mathbf{G}_1\mathbf{O}_1$  is  $\mathcal{O}(N^4 \log N)$  since we have to take the Fourier transform for each column of  $\mathbf{O}_1$ , multiply it with a diagonal matrix  $\mathbf{D}_1$  representing the reciprocal Fresnel propagator and then take the inverse Fourier transform to get the real space result. Computing  $\mathbf{O}_2\mathbf{G}_1\mathbf{O}_1$  is  $\mathcal{O}(N^4)$ . Repeating these steps for  $L$  slices gives the total

Table 3: Estimation of the mean inner potential  $V_0^{\text{Det}}$  from the determinant of the transmission matrix using (14) in comparison to literature values from simulated ( $V_0^{\text{DFT}}$ ) and experimental ( $V_0^{\text{Exp}}$ ) data.

Material	$V_0^{\text{DFT}}$ (V)	$V_0^{\text{Exp}}$ (V)	$V_0^{\text{Det}}$ (V)
GaAs	14.19 [25]	$14.24 \pm 0.08$ [24] [25] $14.53 \pm 0.17$ [25, 26], 13.2 [27]	12.50 (sim.)
SrTiO <sub>3</sub>	SrO 15.2, TiO <sub>2</sub> 17.7 [28, 29]	SrO 13.3, TiO <sub>2</sub> 14.6 [28, 29]	19.28 (sim.)
Au	28.40 [30]	30.2 [31], 21.2 [32], 22 – 27 [33] 16.8 [34], 21.4 [35], 25 [36] 32.2 [37]	28.37 (sim.)
MoS <sub>2</sub>	10.6 [38]	10.4 [38]	10.83 (exp.)

complexity of  $\mathcal{O}(LN^4 \log N)$  operations, which is more efficient compared to the construction of the scattering matrix.

## 6 Conclusion

In this study, we discussed a new perspective for analyzing and understanding the relationship between the multislice and Bloch wave methods. Our presented reformulation of the multislice method into a matrix framework, which we call transmission matrix, not only enables leveraging eigenstructure analysis to measure the similarity with the scattering matrix but also the estimation of the mean inner potential of crystalline materials from diffraction data. By expressing the multislice method as the transmission matrix, we have demonstrated that its structure parallels that of the scattering matrix. Firstly we demonstrate mathematically that the eigenvalues of both matrices are equal up to an additive multiple of  $2\pi$ . Secondly, we prove that the eigenvectors are interconnected through the two-dimensional Fourier matrix, with the eigenvector of the transmission matrix representing the Bloch wave itself in real space. Our matrix-based approach allows the approximation of the projected potential of the material. Moreover, our numerical evaluations of plane-wave diffraction, eigenvalues, as well as projected and mean inner potential support these theoretical results, confirming the robustness and accuracy of the theoretical derivation of eigenstructures for both the transmission and scattering matrix. Additionally, the structure of the transmission matrix makes it possible to utilize the determinant, i.e., the product of all eigenvalues, to estimate the mean inner potential of crystalline materials, thus making it a convenient tool for the evaluation of practical experiments, particularly due to its lower computational demands relative to the scattering matrix of the Bloch wave approach.

## References

- [1] Hans Bethe, “Theorie der Beugung von Elektronen an Kristallen,” *Annalen der Physik*, vol. 392, no. 17, pp. 55–129, 1928.
- [2] John Maxwell Cowley and Alexander Forbes Moodie, “The scattering of electrons by atoms and crystals. I. A new theoretical approach,” *Acta Crystallographica*, vol. 10, no. 10, pp. 609–619, 1957.
- [3] Kazuo Ishizuka and Natsu Uyeda, “A new theoretical and practical approach to the multislice method,” *Acta Crystallographica Section A: Crystal Physics, Diffraction, Theoretical and General Crystallography*, vol. 33, no. 5, pp. 740–749, 1977.
- [4] Dirk Van Dyck, “Fast computational procedures for the simulation of structure images in complex or disordered crystals: a new approach,” *Journal of Microscopy*, vol. 119, no. 1, pp. 141–152, 1980.
- [5] P Goodman and Alexander Forbes Moodie, “Numerical evaluations of N-beam wave functions in electron scattering by the multi-slice method,” *Acta Crystallographica Section A: Crystal Physics, Diffraction, Theoretical and General Crystallography*, vol. 30, no. 2, pp. 280–290, 1974.
- [6] Lorenzo Sturkey, “The calculation of electron diffraction intensities,” *Proceedings of the Physical Society*, vol. 80, no. 2, pp. 321, 1962.
- [7] Fuminori Fujimoto, “Dynamical theory of electron diffraction in Laue-case, I. general theory,” *Journal of the Physical Society of Japan*, vol. 14, no. 11, pp. 1558–1568, 1959.

- [8] Les J Allen, H Leeb, and AEC Spargo, “Retrieval of the projected potential by inversion from the scattering matrix in electron–crystal scattering,” *Acta Crystallographica Section A: Foundations of Crystallography*, vol. 55, no. 2, pp. 105–111, 1999.
- [9] John CH Spence, B Calef, and Jian-Min Zuo, “Dynamic inversion by the method of generalized projections,” *Acta Crystallographica Section A: Foundations of Crystallography*, vol. 55, no. 2, pp. 112–118, 1999.
- [10] Andrew M Maiden, Martin J Humphry, and John M Rodenburg, “Ptychographic transmission microscopy in three dimensions using a multi-slice approach,” *Journal of the Optical Society of America A*, vol. 29, no. 8, pp. 1606–1614, 2012.
- [11] Hamish G Brown, Zhen Chen, Matthew Weyland, Colin Ophus, Jim Ciston, Les J Allen, and Scott D Findlay, “Structure retrieval at atomic resolution in the presence of multiple scattering of the electron probe,” *Physical Review Letters*, vol. 121, no. 26, pp. 266102, 2018.
- [12] Jeffrey J Donatelli and John CH Spence, “Inversion of many-beam Bragg intensities for phasing by iterated projections: Removal of multiple scattering artifacts from diffraction data,” *Physical Review Letters*, vol. 125, no. 6, pp. 065502, 2020.
- [13] Scott D Findlay, Hamish G Brown, Philipp M Pelz, Colin Ophus, Jim Ciston, and Les J Allen, “Scattering matrix determination in crystalline materials from 4D scanning transmission electron microscopy at a single defocus value,” *Microscopy and Microanalysis*, vol. 27, no. 4, pp. 744–757, 2021.
- [14] Zhen Chen, Yi Jiang, Yu-Tsun Shao, Megan E Holtz, Michal Odstrčil, Manuel Guizar-Sicairos, Isabelle Hanke, Steffen Ganschow, Darrell G Schlom, and David A Muller, “Electron ptychography achieves atomic-resolution limits set by lattice vibrations,” *Science*, vol. 372, no. 6544, pp. 826–831, 2021.
- [15] Arya Bangun, Oleh Melnyk, Benjamin März, Benedikt Diederichs, Alexander Clausen, Dieter Weber, Frank Filbir, and Knut Müller-Caspary, “Inverse multislice ptychography by layer-wise optimisation and sparse matrix decomposition,” *IEEE Transactions on Computational Imaging*, vol. 8, pp. 996–1011, 2022.
- [16] Alireza Sadri and Scott D Findlay, “Determining the projected crystal structure from four-dimensional scanning transmission electron microscopy via the scattering matrix,” *Microscopy and Microanalysis*, vol. 29, no. 3, pp. 967–982, 2023.
- [17] Marc De Graef, *Introduction to conventional transmission electron microscopy*, Cambridge University Press, 2003.
- [18] Yi Yang, Qibin Yang, Jianyu Huang, Canying Cai, and Jianguo Lin, “Quantitative comparison between real space and Bloch wave methods in image simulation,” *Micron*, vol. 100, pp. 73–78, 2017.
- [19] P G Self, Michael A O’keefe, Peter R Buseck, and AEC Spargo, “Practical computation of amplitudes and phases in electron diffraction,” *Ultramicroscopy*, vol. 11, no. 1, pp. 35–52, 1983.
- [20] Christoph Koch and Jian-Min Zuo, “Comparison of multislice computer programs for electron scattering simulations and the Bloch wave method,” *Microscopy and Microanalysis*, vol. 6, no. S2, pp. 126–127, 2000.
- [21] Daniel B Durham, Colin Ophus, Khalid M Siddiqui, Andrew M Minor, and Daniele Filippetto, “Accurate quantification of lattice temperature dynamics from ultrafast electron diffraction of single-crystal films using dynamical scattering simulations,” *Structural Dynamics*, vol. 9, no. 6, 2022.
- [22] A J F Metherell, “Diffraction of electrons by perfect crystals,” *Electron Microscopy in Materials Science, part 2*, vol. 397, 1976.
- [23] Colin John Humphreys, “The scattering of fast electrons by crystals,” *Reports on Progress in Physics*, vol. 42, no. 11, pp. 1825, 1979.

- [24] P Kruse, Andreas Rosenauer, and Dagmar Gerthsen, “Determination of the mean inner potential in III–V semiconductors by electron holography,” *Ultramicroscopy*, vol. 96, no. 1, pp. 11–16, 2003.
- [25] P Kruse, Marco Schowalter, Dirk Lamoen, Andreas Rosenauer, and Dagmar Gerthsen, “Determination of the mean inner potential in III–V semiconductors, Si and Ge by density functional theory and electron holography,” *Ultramicroscopy*, vol. 106, no. 2, pp. 105–113, 2006.
- [26] Marija Gajdardziska-Josifovska, Martha R McCartney, WJ De Ruijter, David J Smith, JK Weiss, and Jian-Min Zuo, “Accurate measurements of mean inner potential of crystal wedges using digital electron holograms,” *Ultramicroscopy*, vol. 50, no. 3, pp. 285–299, 1993.
- [27] N Yamamoto and John CH Spence, “Surface imaging of III–V semiconductors by reflection electron microscopy and inner potential measurements,” *MRS Online Proceedings Library (OPL)*, vol. 18, pp. 43, 1982.
- [28] Christopher A Mizzi and Laurence D Marks, “The role of surfaces in flexoelectricity,” *Journal of Applied Physics*, vol. 129, no. 22, 2021.
- [29] Haoying Sun, ZW Mao, TW Zhang, Lu Han, TT Zhang, Xiangbin Cai, Xuyun Guo, Yingfei Li, YP Zang, Wei Guo, et al., “Chemically specific termination control of oxide interfaces via layer-by-layer mean inner potential engineering,” *Nature Communications*, vol. 9, no. 1, pp. 2965, 2018.
- [30] Avi Auslender, Nivedita Pandey, Amit Kohn, and Oswaldo Diéguez, “Mean inner potential of elemental crystals from density-functional theory calculations: Efficient computation and trends,” *Ultramicroscopy*, vol. 255, pp. 113862, 2024.
- [31] VFG Tull, “Some experimental measurements of the inner potentials of various crystals,” *Proceedings of the Royal Society of London. Series A. Mathematical and Physical Sciences*, vol. 206, no. 1085, pp. 219–232, 1951.
- [32] R Buhl, “Interferenzmikroskopie mit Elektronenwellen,” *Zeitschrift für Physik*, vol. 155, pp. 395–412, 1959.
- [33] Max Keller, “Ein Biprisma-Interferometer für Elektronenwellen und seine Anwendung,” *Zeitschrift für Physik*, vol. 164, pp. 274–291, 1961.
- [34] Egon Kerschbaumer, “Ein Biprisma-Interferometer für 100 keV Elektronen und seine Anwendung,” *Zeitschrift für Physik*, vol. 201, no. 2, pp. 200–208, 1967.
- [35] A Goswami and ND Lisgarten, “The measurement of inner potentials for copper, silver and gold,” *Journal of Physics C: Solid State Physics*, vol. 15, no. 19, pp. 4217, 1982.
- [36] Kazuyuki Okazaki, Satoshi Ichikawa, Yasushi Maeda, Masatake Haruta, and Masanori Kohyama, “Electronic structures of Au supported on TiO<sub>2</sub>,” *Applied Catalysis A: General*, vol. 291, no. 1-2, pp. 45–54, 2005.
- [37] Radian Popescu, Erich Müller, Matthias Wanner, Dagmar Gerthsen, Marco Schowalter, Andreas Rosenauer, Artur Böttcher, Daniel Löffler, and Patrick Weis, “Increase of the mean inner Coulomb potential in Au clusters induced by surface tension and its implication for electron scattering,” *Physical Review B — Condensed Matter and Materials Physics*, vol. 76, no. 23, pp. 235411, 2007.
- [38] Victor Boureau, Benoit Sklenard, Robert McLeod, Dmitry Ovchinnikov, Dumitru Dumcenco, Andras Kis, and David Cooper, “Quantitative mapping of the charge density in a monolayer of MoS<sub>2</sub> at atomic resolution by off-axis electron holography,” *ACS nano*, vol. 14, no. 1, pp. 524–530, 2019.
- [39] Ralph Wyckoff, *Crystal Structures*, vol. 2, Interscience Publishers, New York, 1963.
- [40] Roger H Mitchell, Anton R Chakhmouradian, and Patrick M Woodward, “Crystal chemistry of perovskite-type compounds in the tausonite-loparite series, (Sr<sub>1–2x</sub>Na<sub>x</sub>La<sub>x</sub>)TiO<sub>3</sub>,” *Physics and Chemistry of Minerals*, vol. 27, no. 8, pp. 583–589, 2000.
- [41] Anil K Jain, *Fundamentals of digital image processing*, Prentice-Hall, Inc., 1989.

# A Appendix

This appendix is presented as supplement materials for the main article. We will describe the original multislice formulation, representation of Fourier transform as a matrix, as well as more numerical experiments.

## A.1 Multislice Method

We present the classical formulation of the multislice method and briefly discuss the derivation of the matrix formulation of multislice. The complete derivation is given in [15].

Suppose we have a matrix that represents the  $m$ -th slice from the electrostatic potential of the specimen for a thin slice, similar to (5).

$$\exp\left(i\sigma \int_{z_m}^{z_{m+1}} V(x, y, z) dz\right)$$

In fact, for each combination axis  $x, y$  we collect the potential and construct it into matrix  $\mathbf{X}_m \in \mathbb{C}^{N \times N}$  for a total slice number of  $m \in [M]$ . The interaction between the first slice and the electron wave for focused illumination at a specific scanning point  $s$  is given by

$$\mathbf{E}_1 = \mathbf{X}_1 \circ \mathbf{P}_s \in \mathbb{C}^{N \times N}$$

The exit wave is used as the source for the next slice by propagating it with the Fresnel propagator  $\mathcal{V}$ ,

$$\mathbf{E}_m = \mathcal{V}(\mathbf{E}_{m-1}) \circ \mathbf{X}_m \in \mathbb{C}^{N \times N} \quad \text{for } m \in \{2, 3, \dots, M\}.$$

The Fresnel propagator is given in Fourier space for specific distance parameter between slices. Here we define the Fourier space of the Fresnel propagator matrix  $\mathbf{H}_m \in \mathbb{C}^{N \times N}$ . Its elements are given in (7). Hence, the Fresnel propagation can be written as

$$\mathcal{V}(\mathbf{E}_m) := \mathcal{F}^{-1}(\mathbf{H}_m \circ \mathcal{F}(\mathbf{E}_m))$$

At the end, the intensity recorded at a specific scanning point  $s$  in the microscope's detector plane is given as

$$\mathbf{I}_s = |\mathcal{F}(\mathbf{E}_M)|^2 \in \mathbb{R}^{N \times N},$$

where the absolute value is applied to each element of the matrix.

It can clearly be seen that, separating the entanglement between the electron wave and the object is difficult. Hence, we do not have an exact representation of the transmission function of the object, independent of the propagated exit wave starting from the probe illumination. As discussed in [15], the reformulation by leveraging the property of element-wise or Hadamard matrix product, namely

$$\begin{aligned} \text{vec}(\mathbf{A} \circ \mathbf{B}) &= \text{diag}(\text{vec}(\mathbf{A})) \text{vec}(\mathbf{B}) \\ &= \text{diag}(\text{vec}(\mathbf{B})) \text{vec}(\mathbf{A}), \end{aligned} \tag{15}$$

where the function  $\text{vec} : \mathbb{C}^{N \times N} \mapsto \mathbb{C}^{N^2}$  is used to convert matrix into vector and  $\text{diag} : \mathbb{C}^{N^2} \mapsto \mathbb{C}^{N^2 \times N^2}$  is the function to construct a diagonal matrix from a vector. The vectorized intensity at scanning point  $s$  can be written as

$$\mathbf{i}_s = \left| \mathbf{F}_{2D} \left( \prod_{m=1}^M \mathbf{G}_m \mathbf{O}_m \right) \mathbf{p}_s \right|^2 \in \mathbb{R}^{N^2} \text{ for } s \in [S]$$

Using this formulation we can disentangle the illumination from electron wave and the object to get pure transmission function

$$\mathbf{A} = \prod_{m=1}^M \mathbf{G}_m \mathbf{O}_m,$$

where the formulation of Fresnel matrix  $\mathbf{G}_m$  is derived in (6).

## A.2 Matrix Representation of Fourier Transforms

We present a matrix representation of Fourier transforms. The one-dimensional Fourier transform we can be written as a matrix-vector product. Here, the term one-dimensional Fourier matrix represents the discrete implementation of the Fourier basis, i.e., when we sample the Fourier basis and store it as a matrix  $\mathbf{F}_{1D} \in \mathbb{C}^{N \times N}$ . Hence, the one-dimensional Fourier transform of vector  $\mathbf{x} \in \mathbb{C}^{N \times N}$  can be written as

$$\mathbf{y} = \mathbf{F}_{1D}\mathbf{x},$$

where the one-dimensional Fourier transform is given by [41, eq.5.44],

$$\mathbf{F}_{1D} = \frac{1}{\sqrt{N}} \begin{pmatrix} e^{-\frac{i2\pi f_1 x_1}{N}} & e^{-\frac{i2\pi f_1 x_2}{N}} & \dots & e^{-\frac{i2\pi f_1 x_N}{N}} \\ e^{-\frac{i2\pi f_2 x_1}{N}} & e^{-\frac{i2\pi f_2 x_2}{N}} & \dots & e^{-\frac{i2\pi f_2 x_N}{N}} \\ \vdots & \vdots & \dots & \vdots \\ e^{-\frac{i2\pi f_N x_1}{N}} & e^{-\frac{i2\pi f_N x_2}{N}} & \dots & e^{-\frac{i2\pi f_N x_N}{N}} \end{pmatrix} \in \mathbb{C}^{N \times N}.$$

Here,  $x_j$  for  $j \in [N]$  represents the sampling points at evenly spaced real space coordinates, and  $f_j$  for  $j \in [N]$  is the sample in the Fourier space. Along the same line, the two-dimensional Fourier matrix can be constructed using the Kronecker product between two of the one-dimensional Fourier matrices  $\mathbf{F}_{2D} = \mathbf{F}_{1D} \otimes \mathbf{F}_{1D} \in \mathbb{C}^{N^2 \times N^2}$ . Thereby, the two-dimensional Fourier transform of matrix  $\mathbf{X} \in \mathbb{C}^{N \times N}$  can be written as  $\mathbf{F}_{2D} \text{vec}(\mathbf{X}) \in \mathbb{C}^{N^2}$ .

## A.3 Additional Numerical Experiments

In this section, we present more numerical experiments for several thickness of diffraction patterns related to Figure 3, phase of eigenvalues as in Figure 5, as well as projected potential as in Figure 6.

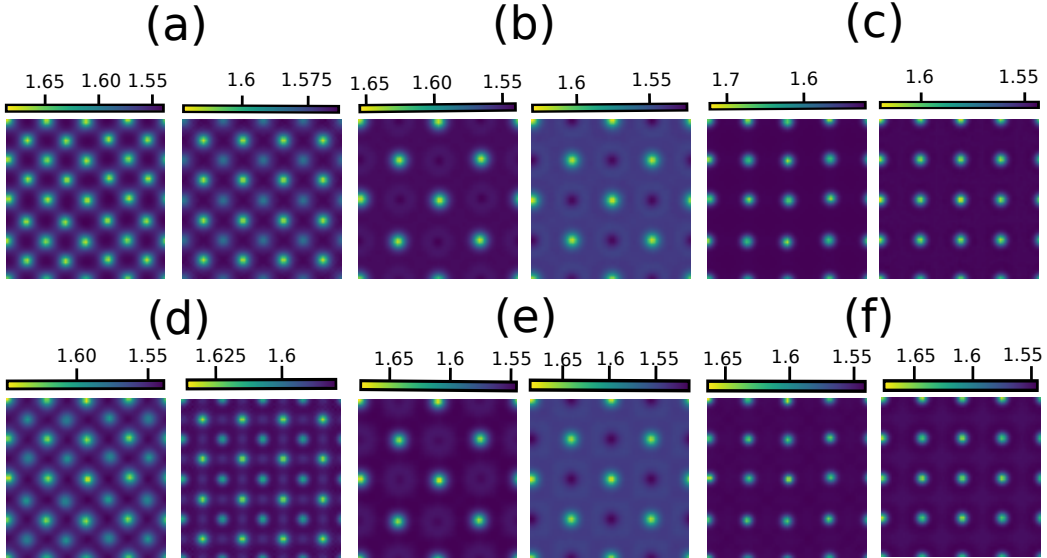


Figure 8: Projected potential of  $2 \times 2$  unit cells in  $[001]$  zone axis of (a), (d) GaAs with thickness  $141.33 \text{ \AA}$  (25 unit cells) and  $197.87 \text{ \AA}$  (35 unit cells), (b), (e)  $\text{SrTiO}_3$  with thickness  $39.05 \text{ \AA}$  (10 unit cells) and  $58.58 \text{ \AA}$  (15 unit cells), (c), (f) Au with thickness  $20.4 \text{ \AA}$  (5 unit cells) and  $40.8 \text{ \AA}$  (10 unit cells). Left figure is calculated with the transmission matrix, and the right figure with the scattering matrix.

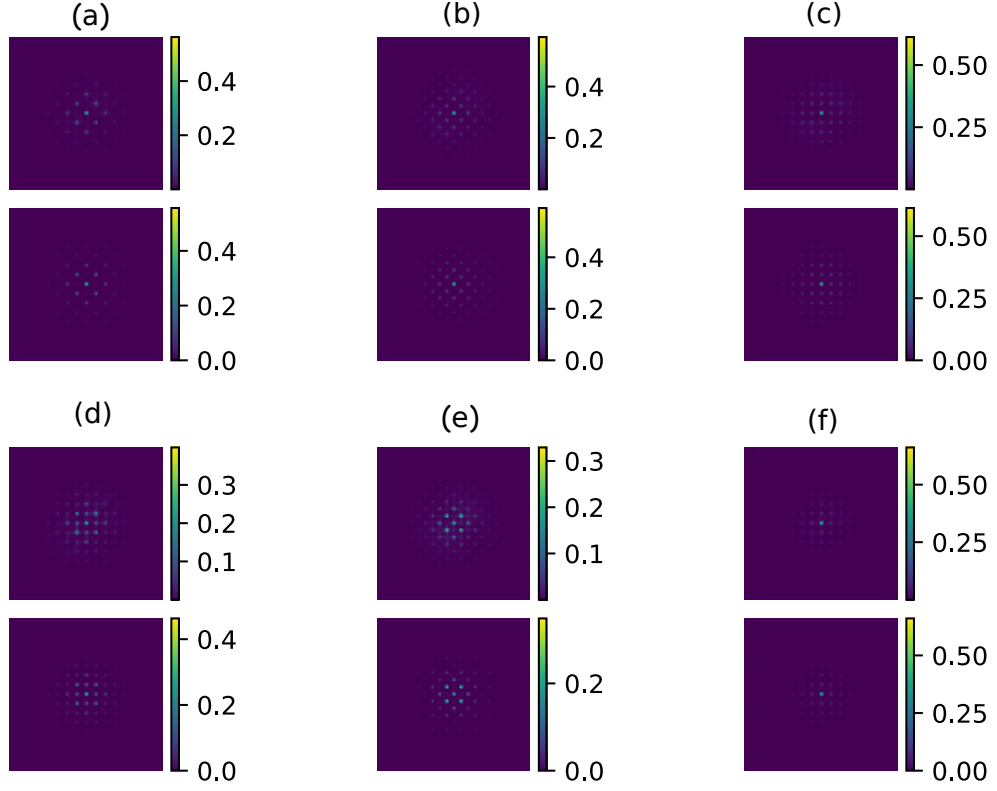


Figure 9: Diffraction patterns along the  $[001]$  zone axis calculated using the transmission matrix (top row) and the scattering matrix (bottom row) for (a), (d) GaAs with simulated thickness  $62.1863 \text{ \AA}$  and  $476.9173 \text{ \AA}$ , (b)  $\text{SrTiO}_3$  with simulated thickness  $44.88 \text{ \AA}$  and  $330.48 \text{ \AA}$ , (c), (f) Au with simulated thickness  $42.955 \text{ \AA}$  and  $316.305 \text{ \AA}$

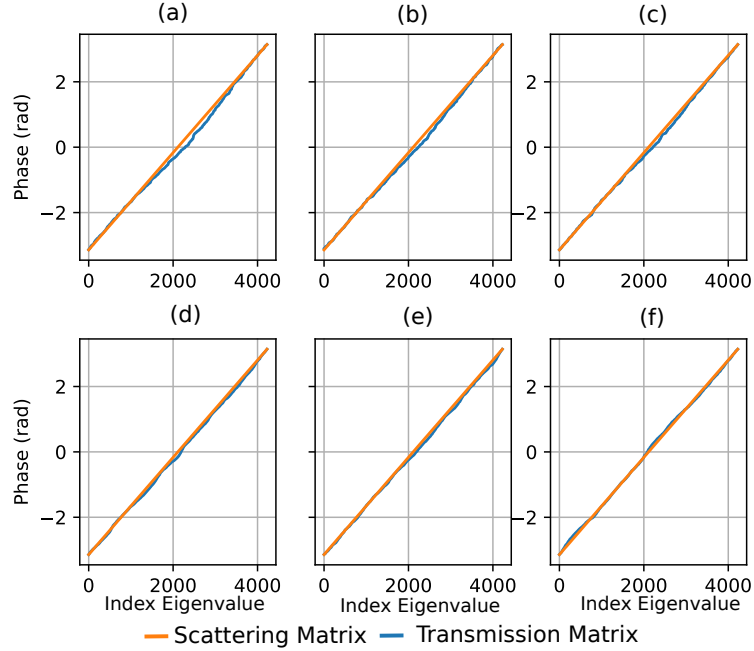


Figure 10: Phase distribution of eigenvalues from both transmission and scattering matrix for (a), (d) GaAs of thickness  $28.27 \text{ \AA}$  with standard deviation (SD) of  $0.098 \text{ rad}$  and thickness  $282.66 \text{ \AA}$  with  $\text{SD} = 0.043 \text{ rad}$ , (b), (e)  $\text{SrTiO}_3$  thickness  $19.525 \text{ \AA}$  with  $\text{SD} = 0.068 \text{ rad}$  and thickness  $195.25 \text{ \AA}$  with  $\text{SD} = 0.0368$ , (c), (f) Au thickness  $20.4 \text{ \AA}$  and  $\text{SD} = 0.06 \text{ rad}$  and thickness  $204 \text{ \AA}$  and  $\text{SD} = 0.05 \text{ rad}$ .